

# Journal of Biomedical Optics

BiomedicalOptics.SPIEDigitalLibrary.org

## **Quantitative performance characterization of three-dimensional noncontact fluorescence molecular tomography**

Rosy Favicchio  
Stylianos Psycharakis  
Kai Schönig  
Dusan Bartsch  
Clio Mamalaki  
Joseph Papamatheakis  
Jorge Ripoll  
Giannis Zacharakis

# Quantitative performance characterization of three-dimensional noncontact fluorescence molecular tomography

Rosy Favicchio,<sup>a,b,c,\*</sup> Stylianos Psycharakis,<sup>b</sup> Kai Schönig,<sup>d</sup> Dusan Bartsch,<sup>d</sup> Clio Mamalaki,<sup>c</sup> Joseph Papamatheakis,<sup>c</sup> Jorge Ripoll,<sup>e,f</sup> and Giannis Zacharakis<sup>b</sup>

<sup>a</sup>Imperial College London, Hammersmith Hospital, Department of Surgery and Cancer, Division of Cancer, Du Cane Road, London W12 0NN, United Kingdom

<sup>b</sup>Foundation for Research and Technology Hellas–Institute of Electronic Structure and Laser, N. Plastira 100, 7100 Heraklion, Crete, Greece

<sup>c</sup>Foundation for Research and Technology Hellas–Institute of Molecular Biology and Biotechnology, N. Plastira 100, 7100 Heraklion, Crete, Greece

<sup>d</sup>Central Institute of Mental Health and Heidelberg University, Department of Molecular Biology, Medical Faculty Mannheim, J5, 68159 Mannheim, Germany

<sup>e</sup>Universidad Carlos III of Madrid, Department of Bioengineering and Aerospace Engineering, 28911 Madrid, Spain

<sup>f</sup>Instituto de Investigación Sanitaria del Hospital Gregorio Marañón, Experimental Medicine and Surgery Unit, 28007 Madrid, Spain

**Abstract.** Fluorescent proteins and dyes are routine tools for biological research to describe the behavior of genes, proteins, and cells, as well as more complex physiological dynamics such as vessel permeability and pharmacokinetics. The use of these probes in whole body *in vivo* imaging would allow extending the range and scope of current biomedical applications and would be of great interest. In order to comply with a wide variety of application demands, *in vivo* imaging platform requirements span from wide spectral coverage to precise quantification capabilities. Fluorescence molecular tomography (FMT) detects and reconstructs in three dimensions the distribution of a fluorophore *in vivo*. Noncontact FMT allows fast scanning of an excitation source and noninvasive measurement of emitted fluorescent light using a virtual array detector operating in free space. Here, a rigorous process is defined that fully characterizes the performance of a custom-built horizontal noncontact FMT setup. Dynamic range, sensitivity, and quantitative accuracy across the visible spectrum were evaluated using fluorophores with emissions between 520 and 660 nm. These results demonstrate that high-performance quantitative three-dimensional visible light FMT allowed the detection of challenging mesenteric lymph nodes *in vivo* and the comparison of spectrally distinct fluorescent reporters in cell culture.

© The Authors. Published by SPIE under a Creative Commons Attribution 3.0 Unported License. Distribution or reproduction of this work in whole or in part requires full attribution of the original publication, including its DOI. [DOI: 10.1117/1.JBO.21.2.026009]

Keywords: molecular imaging; fluorescence molecular tomography; quantification; fluorescent probes.

Paper 150605RR received Sep. 15, 2015; accepted for publication Jan. 13, 2016; published online Feb. 18, 2016.

## 1 Introduction

*In vivo* optical imaging instruments have become mainstream tools for the visualization of molecular function and disease diagnostics. Fluorescence molecular tomography (FMT) offers an advantage over other optical imaging techniques in its ability to accurately quantify fluorescent signal.<sup>1–3</sup> Defining the performance of fluorescence tomography imagers is of primary importance because it is the ability to quantify fluorescent concentration that will spur the development of new biological applications. In FMT technology, fluorescence provides contrast between targeted and nontargeted tissues noninvasively<sup>4</sup> using noncontact detectors.<sup>5–7</sup> For a sample of given optical properties, the emitted intensity is dependent on the distance between the source and the fluorescent object<sup>8</sup> and on the intensity of the excitation beam.<sup>9–11</sup> Tomographic information is obtained at multiple projections, and the variation in fluorescence intensity at each projection is used to extrapolate spatial information.<sup>12–14</sup> FMT image reconstruction computes the concentration of a fluorophore and its volume, making some assumptions about its

absorption and scattering coefficients,<sup>15,16</sup> knowing the sample thickness,<sup>17</sup> and experimentally measuring the normalized Born approximation<sup>18</sup> to retrieve the position, shape, and concentration of a target fluorophore.<sup>19</sup> A three-dimensional (3-D) image is generated by creating a weight matrix of the sample, where voxel intensity values are assigned iteratively.<sup>15,20–22</sup> However, in biological research, measuring fluorescence is effectively performed in a semiquantitative manner, and it is necessary for the user to define an “application-tailored” signal-to-noise ratio (SNR) and choose fluorophores based on the properties of the imager. From the user’s perspective, fluorescence emission intensity depends on the following variables: excitation intensity,<sup>23</sup> spectral characteristics of the target fluorophore,<sup>2,24</sup> spectral properties of the tissue sampled,<sup>25</sup> and bandpass filters used; and it is ultimately proportional to fluorophore concentration. It follows that if the variable parameters can be controlled, emission can be measured consistently and the diffusion approximation<sup>11,22</sup> solved for fluorophore concentration. As the major absorber of visible light in living organisms, hemoglobin plays a crucial role in light transmission and imaging gene activity effectively *in vivo*, beyond 600 nm is highly desirable; however, the number of applications using NIR fluorescent proteins is still small. The need to evaluate true *in vivo*

\*Address all correspondence to: Rosy Favicchio, E-mail: [r.favicchio@imperial.ac.uk](mailto:r.favicchio@imperial.ac.uk)

performance of fluorescent proteins (FPs) within the visible spectral window is thereby crucial, given that the choice of unsuitable reporter fluorophores could lead to inaccurate results independent of FMT imager performance.

Here, the capabilities and limitations of a custom-built noncontact FMT system in localizing and quantifying fluorescent signal under variable experimental conditions were evaluated *in vitro*, in cell culture, and *in vivo*. To this purpose, we made use of a Tet-ON conditional gene expression system<sup>26</sup> where five FPs were cloned in stable cell lines within the same genetic locus, thus resulting in identical mRNA expression levels. Since promoter activity was equal, it follows that variability in fluorescence emission intensity could be directly related to the activity of each FP (including brightness, stability, cell toxicity, and so on). *In vivo* validation of the FMT detection sensitivity was tested by targeting subcutaneous and deep-seated lymph nodes (LNs) in a transgenic mouse model. The FMT was used to quantify the T-cell population,<sup>27</sup> focusing on how to overcome the practical challenges of detecting fluorescence from different anatomical locations. These data provide essential information for application design by establishing the quantitative accuracy, standardization, and reproducibility of the FMT imager. A calibration method was further established that enabled conversion of FMT signal intensity to molarity. In conclusion, these data describe a set of methodological steps that validate noncontact free-space fluorescence tomography *in vitro* and *in vivo* as an accurate technique for the detection and quantitative comparison of spectrally distinct fluorophores emitting between 520 and 660 nm.

## 2 Materials and Methods

### 2.1 Experimental Setup

The experimental noncontact FMT setup used [Fig. 1(a)] employed a continuous-wave argon-ion laser source (LaserPhysics, Reliant 1000m, West Jordan, Utah) emitting at 457, 488, and 514 nm and enclosed in a custom-built aluminum chamber coated in antireflective black coating (deep black optical paint, Gerd Neumann, Hamburg, Germany). The source was directed across three fixed mirrors (High Energy Argon-Ion Laser Mirrors, Edmund Optics, Barrington, Illinois) and a UV-NIR neutral density filter (Edmund Optics) into the FMT chamber and onto an optical scanner employing galvo-mirrors (Scanlab, SCANcube 7, Munich, Germany). Incident light power was measured before entering the optical scanner using a laser power meter (PH100-Si-OD2, Gentec Electro-Optics). The setup was designed to operate in both transmission and reflection geometries by repositioning a mirror (First Surface mirror, Edmund Optics) mounted on a travel linear translation stage (Edmund Optics). The sample holder was mounted on an electronically controlled  $x-y-z$  positioning stage (Standa, Vilnius, Lithuania). A custom-built filter wheel accommodating up to five filters was aligned to a 50 mm Macro f/2.8 objective (SIGMA Corporation, Tokyo, Japan). Light collection was performed using a 510/10-, 540/40-, 593/40-, or 615/90-nm interference bandpass filters (Andover Corporation, Salem, New Hampshire) to isolate fluorescence from excitation light. A 16-bit, 1024 × 1024 pixel charge-coupled device (CCD) (DV 434, Andor Technology, Belfast, Northern Ireland), thermoelectrically cooled down to  $-65^{\circ}\text{C}$ , was used for the detection of signals. The lens was focused on the surface of the sample, and the image scaled from pixel dimensions to

metric units by the use of metric fiducials. Stage calibration was performed to convert the CCD field of view to degrees of rotation of the galvo-mirrors. For all experiments, an image was obtained with white light illumination before exposure to the laser source and was used as a reference image for source pattern selection. Additionally, a background image in the absence of an illuminating source was acquired to account for any external light entering the FMT chamber. Illumination sources were distributed symmetrically to the target location for both reproducibility and calibration experiments. Exposure time used was 0.2 s with 0.8 mW excitation power. Identical source/detector parameters were used for the fluorophores Atto590 (excitation max 594 nm, emission max 624 nm; ATTO-TEC GmbH, Germany) and carboxyfluorescein succidimyl ester (CFSE) (excitation max 492 nm, emission max 517 nm; Thermo Fisher Scientific Inc.) placed in a 2-mm capillary glass tube in a phantom at a depth of 3 mm from the surface. A slab geometry phantom was used with a combination of 20 ppm India ink and 1% Intralipid-20% to match tissue-like optical properties at 520 nm (scattering coefficient  $\mu_s = 16 \text{ cm}^{-1}$  and absorption coefficient  $\mu_a = 0.3 \text{ cm}^{-1}$ ) and at a depth of 12 mm. An isoflurane vaporizer was used to deliver anesthetic to the FMT chamber and to the induction chamber, and a scavenging system was used to remove excess anesthetic gas (Fluovac systems, Harvard Apparatus, Holliston, Massachusetts).

### 2.2 Tomographic Data Acquisition and Reconstruction

Tomographic imaging was performed by scanning the laser source into selected illumination points.<sup>23</sup> The optimum excitation source pattern found for the tomographic scans was an  $8 \times 8$  grid covering a field of view of  $12 \times 12$  mm. For each illumination point, two measurements (excitation and emission) were recorded sequentially with the appropriate bandpass filters placed in front of the CCD. An image stack was created for all illumination points creating two sets of raw data (excitation and emission). Excitation and emission stacks were then resampled to a  $14 \times 14$  detector grid covering the target area and used for the tomographic reconstructions. Data from the excitation and emission stacks were used to create the normalized Born ratio<sup>18</sup> as shown in the following equation:

$$U^{\text{NB}} = \frac{U_{\text{fl}}}{U_{\text{exc}}} = W_{\text{fl}} \cdot \text{fluo}(r), \quad (1)$$

where  $U^{\text{NB}}$  is the normalized measurement,  $U_{\text{fl}}$  and  $U_{\text{exc}}$  are the background corrected fluorescence and excitation measurements,  $W_{\text{fl}}$  is the weight matrix describing the light propagation through the specific medium, and  $\text{fluo}(r)$  is the fluorescence concentration. The 3-D reconstruction [Figs. 1(b)–1(e)] was performed using diffusion theory and modeling light propagation<sup>16</sup> in free space<sup>5</sup> in a homogenous slab solution.<sup>8,19</sup> The tissue medium below the detector area was discretized to a total of 2700 voxels of  $1 \text{ mm} \times 1 \text{ mm} \times 1 \text{ mm}$  centered to the target area. Data inversion was performed using an iterative approach,<sup>20,21,28</sup> and 3-D reconstructions were obtained with 100 iterations (Table 1). For phantom experiments, a cylindrical region of interest (ROI) was selected and the mean intensity value was used for quantification. Variation of the number of iterations did not affect the ROI mean. The source/detector patterns used in transmission geometry were identical to those in reflection modality (10 mW excitation power and 2 s exposure

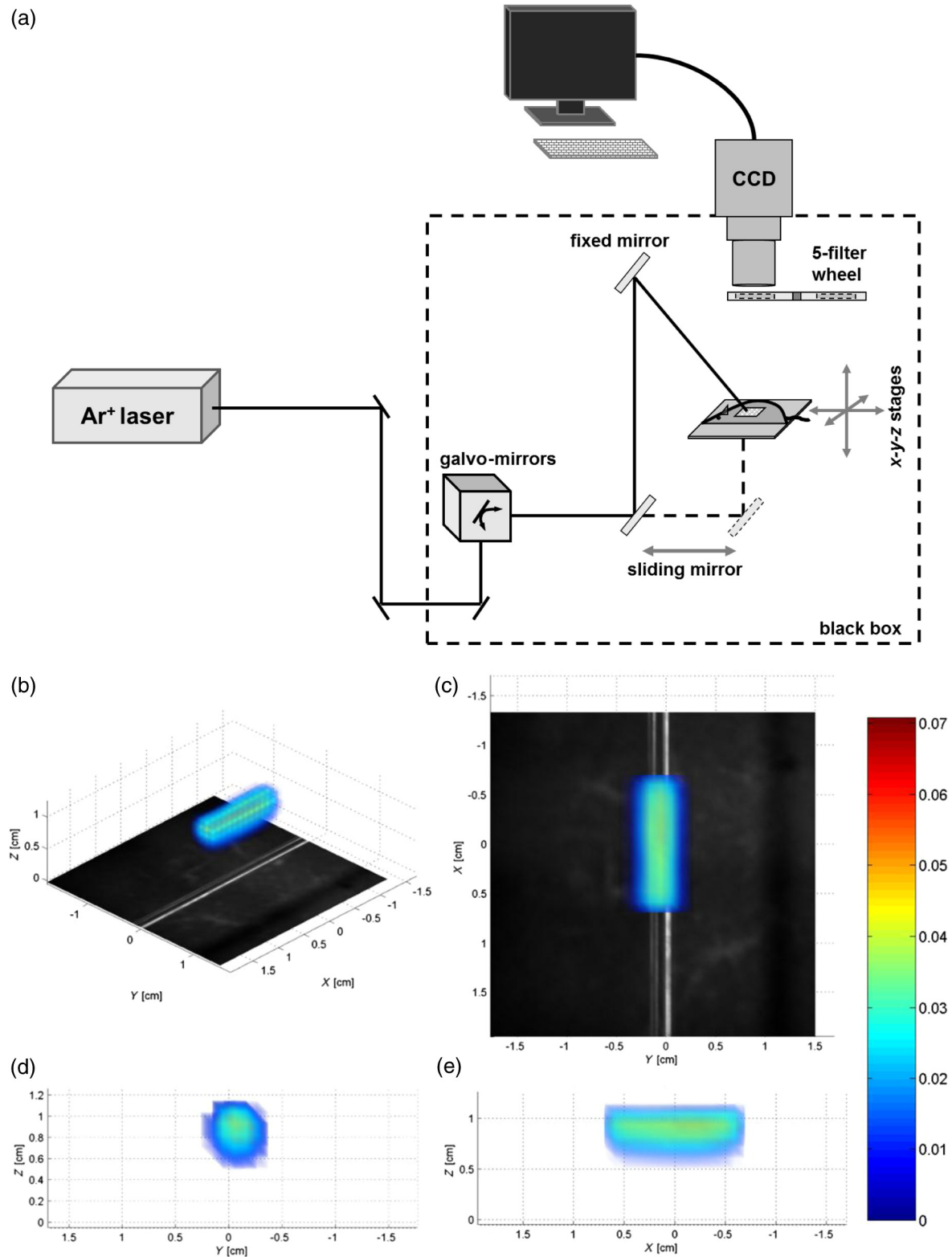


**Fig. 1** Horizontal noncontact FMT imaging system. (a) The FMT setup is illustrated, where the argon-ion source directs the beam into the FMT chamber via two fixed mirrors and into a scan cube that directs the beam via galvo-mirrors onto different user-selected source positions on the sample. The laser source can be directed onto the sample in reflection or transmission geometry by the use of a sliding mirror. Light is collected by a CCD camera, where wavelength is selected by the use of bandpass filters placed on a filter wheel. The data are recorded by a PC. The FMT imager was used to image a phantom containing a glass capillary tube filled with  $10\text{-}\mu\text{M}$  CFSE. (b) 3-D reconstructed image of the capillary tube was obtained with 100 iterations; the tube was clearly visible and geometrically correctly reconstructed. (c) The  $x - y$  plane showed the reconstructed tube in line with its true location, visible in the background image, and 2 mm below the surface. (d) The  $y - z$  plane and (e)  $x - z$  plane images demonstrated that the FMT software correctly reconstructed the tube as a cylindrical object with a homogeneous fluorescent signal.

**Table 1** Comparative statistical analysis for quantification experiments in reflection (R) and transmission (T) modalities. Phantoms with increasing concentrations of CFSE and Atto590 were imaged with the FMT and emission quantified for each dataset. The correlation between the linear regression model used and the experimental data points is illustrated by the  $R^2$  and SDM values. The slope values were used as means to compare reproducibility between modalities. Increasing the number of iterations from 100 to 1000 marginally improves the fits (bold) and the slope. Small differences in slope values can be noticed between reflection and transmission experiments, indicating that a quantitative comparison of values between modalities is possible but may be affected by the intensity range.

Fluorophore	Mode	Iterations	$R^2$	SDM	$N$	Slope
CFSE	R	100	0.99811	$1.01172 \times 10^{-4}$	4	$5.1966 \times 10^{-4}$
CFSE	R	1000	<b>0.99981</b>	$3.8746 \times 10^{-5}$	4	$6.3025 \times 10^{-4}$
CFSE	T	100	0.98518	$4.06563 \times 10^{-4}$	4	$7.41105 \times 10^{-4}$
CFSE	T	1000	<b>0.98463</b>	$4.39479 \times 10^{-4}$	4	$7.8644 \times 10^{-4}$
Atto590	R	100	0.97909	$2.5702 \times 10^{-4}$	4	$2.22456 \times 10^{-4}$
Atto590	R	1000	<b>0.98412</b>	$1.89737 \times 10^{-4}$	4	$2.32 \times 10^{-4}$
Atto590	T	100	0.99628	$1.08321 \times 10^{-4}$	4	$2.2411 \times 10^{-4}$
Atto590	T	1000	<b>0.99738</b>	$1.02355 \times 10^{-4}$	4	$2.52562 \times 10^{-4}$

time). Data acquisition and processing were performed on a 3.0 GHz Pentium D with 512 MB RAM, and the system was controlled by custom-built software using LabView (National Instruments, Austin, Texas) system design software.

### 2.3 Fluorescence Molecular Tomography Calibration

Fluorophore quantum yield (QY) defines the efficiency with which absorbed light is converted to emitted light. Published QYs, however, are recorded at excitation and emission maxima. Such conditions often fail to match experimental conditions due to the wavelengths available and also because experimentally the QY is affected by concentration range and solvent properties. Commercial QY values therefore could not be used for FMT imaging calibration; we used the linear quantification data from CFSE and Atto590 to calculate the FMT-fluorescence yield (FMT-FY) described for our samples and experimental parameters. A plot of FMT-recorded intensities ( $F$ ) (y-axis) against measured sample absorbance  $A$  (x-axis) (FluoroMax, Jobin Yvon, Horiba Scientific, Kyoto, Japan) was obtained by multiplying the known fluorophore concentrations ( $c$ ) by their published extinction coefficient values ( $\epsilon$ ) and measured light path length ( $l$ ) following Beer-Lambert's law:

$$A = \epsilon \cdot c \cdot l. \quad (2)$$

For CFSE,  $\epsilon_{488} = 59,668$ .

For Atto590,  $\epsilon_{514} = 12,000$ .

The absorbance values were then plotted and fitted to a linear regression model, as shown in Fig. 2. The slope of the fits ( $m$ ) is proportional to the QY of the fluorophore, where  $b$  is the intercept on the y-axis:

For CFSE,  $m = 1.27 \times 10^{-8}$ ,  $b = 0$ ; and

For Atto590,  $m = 2.25 \times 10^{-8}$ ,  $b = 9.50 \times 10^{-4}$ .

FMT-FY values were calculated using a standard (st) solution as reference; FMT-FY <sub>$x$</sub>  is thus always expressed as relative to FMT-FY<sub>st</sub> as follows:

$$\phi_x = \phi_{st} \left( \frac{m_x}{m_{st}} \right) \left( \frac{\eta_x^2}{\eta_{st}^2} \right), \quad (3)$$

where  $\phi$  is the FMT-FY of, relatively, the sample ( $\phi_x$ ) and the standard ( $\phi_{st}$ ), and  $\eta$  is the refractive index of the solvent. We calculated the FMT-FY for CFSE ( $\phi_{CFSE}$ ) and Atto590 ( $\phi_{Atto}$ ) using the published QY values as  $\phi_{st}$ , corrected for the wavelengths used:

For CFSE,  $\phi_{max} = 0.80$ ,  $\phi_{488,540} = 0.40$ ; and

For Atto590,  $\phi_{max} = 0.80$ ,  $\phi_{514,615} = 0.08$ .

The calculated FMT-FY for CFSE and Atto590 was

$$\phi_{CFSE} = 0.45, \quad \phi_{Atto590} = 0.70.$$

The ratio of the calculated FMT-FYs ( $\phi$ ) was then compared with the ratio between the slopes ( $m$ ):

$$\frac{\phi_{CFSE}}{\phi_{Atto}} = \frac{0.45}{0.70} = 0.635,$$

$$\frac{m_{CFSE}}{m_{Atto}} = \frac{1.27e^{-8}}{2.25e^{-8}} = 0.563,$$

$$\frac{\phi_{Atto}}{\phi_{CFSE}} = \frac{0.70}{0.45} = 0.157,$$

$$\frac{m_{Atto}}{m_{CFSE}} = \frac{2.25e^{-8}}{1.27e^{-8}} = 0.177.$$

The calculated slopes were proportional to the FMT-FYs and consequently to the fluorophores' QYs (within 10% error). The linear relationship between fluorescence emission intensity and concentration [Eq. (4)] therefore becomes:

$$F = m * \epsilon * c + b, \quad (4)$$

where  $F$  is the fluorescence emission intensity detected by the FMT,  $m$  is the slope of the fit, and  $b$  is the intercept of the linear fit. The slope of each fit ( $m$ ), specific for each fluorophore ( $\epsilon$ ), could therefore be used as a "calibration factor" for the FMT

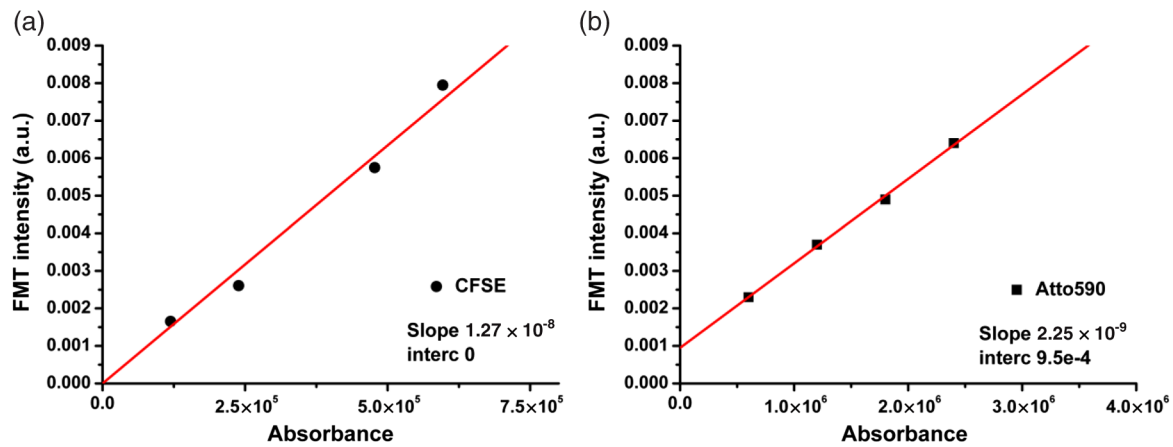


**Fig. 2** FMT calibration. FMT-FY was calculated by converting CFSE and Atto590 concentrations into absorbance values. FMT intensity values were plotted against measured absorbance value ( $A = \epsilon * c * l$ ) for four concentrations of (a) CFSE and (b) Atto590. The points were fitted to a linear regression model, and the slope and intercept points were used to calculate the relative FMT-FY value.

system. Dividing the FMT recorded intensities by ( $m * \epsilon$ ) recovered the FMT concentration values. The details are provided in Table 2.

## 2.4 Cell Culture

Stable HeLa cell lines expressing enhanced yellow fluorescent protein (EYFP), super green fluorescent protein (SGFP), enhanced green fluorescent protein (EGFP), Katushka,<sup>29</sup> or Cardinal<sup>30</sup> red fluorescent protein were generated and characterized as described by Weidenfeld et al.<sup>26</sup> In brief, HeLa Tet-ON advanced cells (line EM2-11ht) were stably transfected with DNA coding for the fluorescent proteins under control of a tetracycline/doxycycline inducible promoter (Ptet). The gene of interest was stably integrated into a defined genomic locus (5q31), which allows tight regulation of the doxycycline-inducible expression. Constructs were inserted by

**Table 2** Conversion table. The molar concentrations of CFSE and Atto590 used and the intensity values (a.u.) recovered from the 3D-FMT data analysis are shown. FMT concentration values represent the converted a.u. units to molarity obtained by the FMT calibration step.

	FMT intensity	FMT concentration
CFSE concentration ( $\mu$ M)		
2	0.00165	2.18
4	0.00261	3.45
8	0.00575	7.60
10	0.00795	10.50
Atto590 concentration ( $\mu$ M)		
5	0.00135	5.00
10	0.00275	10.18
15	0.00395	14.62
20	0.00545	20.18

Flippase Recombinase-Mediated Cassette Exchange (Flp-RMCE), and clonal lines were isolated. The expression characteristics of the derived cell lines were directly comparable as the transgenes were directionally integrated as single copies at the same locus. HeLa cells were cultured in DMEM supplemented with 10% FBS, 2 mM glutamine, and 1% penicillin/streptomycin. Expression of SGFP, EGFP, EYFP, Katushka, or Cardinal was induced by doxycycline, supplied to the media at 200 ng/ml. For FMT imaging of HeLa monolayers, 24-well tissue culture plates were used.

## 2.5 Animals

Rag1<sup>-/-</sup>,<sup>31,32</sup> CD2,<sup>33</sup> and DsRed<sup>34</sup> transgenic animals were maintained in the Institute of Molecular Biology and Biotechnology colony. For the FMT imaging, the animals ( $n = 4$ ) were anesthetized with 1.5% isoflurane, initially delivered at 2.5% in a tranquilizing chamber. Temperature and breathing of each animal were monitored during the experimental procedure. Mesenteric nodes (MNs) were detected after feeding the mice for 2 weeks with alfalfa-free food (Labdiet), and hair was removed using depilatory cream. All animal experimental protocols were conducted in accordance with and under the approval of the Foundation for Research and Technology Ethics Committee and the General Directorate of Veterinary Services, Region Crete (permit numbers: EL 91BIO-02 and EL91-BIOexp-02).

## 2.6 Cell Culture Experimental Protocol

A 24-well cell culture plate containing HeLa-*wt* and stable HeLa clones expressing either EGFP, EYFP, SGFP, Katushka, or Cardinal ( $n = 3$ ) was imaged using a two-dimensional (2-D) raster scan, ensuring homogeneous excitation across samples. The EGFP-, SGFP-, and EYFP-positive cells were excited using the 488-nm laser line, and emission was recorded with 510/10-nm and a 540/40-nm filters. Katushka- and Cardinal-positive cells were excited with the 514-nm laser line, and 593/40-nm and 615/90-nm filters were used for emission. SGFP-positive cells were measured with all filter sets. To mimic the high absorbance, freshly heparinated mouse blood was added to the culture wells to a final concentration of 12% (assuming a molar extinction coefficient of 24202.4 [ $\text{cm}^{-1}/(\text{moles/L})$ ] at 520 nm, matching  $\mu_a = 16 \text{ cm}^{-1}$ ). ROI

areas (identical for all samples) corresponding to the width of the wells were used to quantify FP emission. The data were normalized for filter width, excitation, and emission wavelength and for cell number. Fluorimeter data were experimentally measured for each population at  $1 \times 10^6$  cells/mL.

## 2.7 In Vivo Experimental Protocol

Initially, a 2-D scan was performed on each animal to locate the target LN using 514-nm excitation and 615/90-nm emission (1 mW excitation power and 6 s exposure time). These images were used to determine the scan pattern position: a  $10 \times 10$  source grid was chosen to cover a wide field of view ( $2 \times 2$  cm) with 25 mW excitation power and 0.2- to 0.6-s exposure time for the superficial and deep targets, respectively. Tomographic data were recorded using 514-nm excitation with 615/90-nm and a 690/30-nm emission filters for fluorescence measurement and a 510/10-nm filter to measure the excitation field. The data were processed with in-house developed software using a  $10 \times 10$  detector pattern.

## 3 Results

### 3.1 In Vitro Quantification

In order to assess the capabilities of the FMT system, a set of experiments was designed to address its sensitivity, dynamic range, and resolution. Each query was dependent on the SNR and was therefore application dependent. Given that the optical properties of the fluorescent object of interest and its immediate surroundings significantly affected the SNR, each experiment here reported was acquired using settings where the SNR was experimentally maximized. A typical 3-D-reconstructed image is shown in Fig. 1. The FMT imager was tested in reflection and transmission geometry modes at different wavelengths. Initially, response was assessed with phantoms containing 2, 4, 8, and  $10 \mu\text{M}$  of CFSE in reflection geometry. To compare the quantification accuracy at different spectral regions, CFSE was replaced with Atto590. Atto590 has a high molecular absorption and a high QY (0.80); however, the 514-nm source achieved approximately 10% excitation efficiency. This resulted in a 60% weaker Atto590 emission compared with CFSE (excitation

max 489 nm). Atto590 concentrations (5, 10, 15, and  $20 \mu\text{M}$ ) were chosen to match the intensity range used for CFSE. Similarly, a set of experiments assessed the quantification capabilities of the FMT imager in transmission geometry. Quantification of mean intensity values in transmission geometry was achieved using the same reconstruction and ROI parameters used for reflection and were therefore directly comparable. The results from the quantification analysis for CFSE and Atto590 in reflection and transmission modes (Fig. 3) were fitted to a linear regression model (Table 1). The quantification data showed the reconstructed fluorescence mean intensity values to be linearly proportional to fluorescence concentration.

### 3.2 In Vitro Reproducibility

The FMT imager's reproducibility was then assessed by designing a set of *in vitro* experiments carried out in reflection geometry using  $2\text{-}\mu\text{M}$  CFSE. Data acquisition, processing, ROI selection, and quantification were obtained (excitation 488 nm, emission 540/40 nm;  $8 \times 8$  source/detector pattern, 100 iterations) for four independent measurements performed as technical repeats. Reproducibility was assessed by standard deviation of the mean (SDM) and standard error of the mean (SEM),  $1.61334 \times 10^{-5}$  and  $8.0667 \times 10^{-6}$ , respectively, 2 and 3 orders of magnitude smaller than the mean (0.00204 a.u.), with a coefficient of variance of 0.00792 indicating a systemic error  $<0.8\%$ . Conversion using the calibration factor in Eq. (4) recovered a value of  $2.69 \mu\text{M}$ .

### 3.3 Optimal Fluorescent Protein Selection for Fluorescence Molecular Tomography

The intrinsic properties of fluorescent proteins dictate whether or not they are suitable for an application; however, these are seldom explicitly tested. The relative intensities of the emission displayed by identical numbers of HeLa cells expressing YFP, SGFP, EGFP, Katushka, or Cardinal were obtained by quantifying the mean FMT reconstructed values. The mean intensity values recorded [Figs. 4(a) and 4(b)] were corrected for filter width. These normalized data give a more accurate intensity value for each fluorophore considered; more precisely, they represent a weighted average across the filter wavelength range.

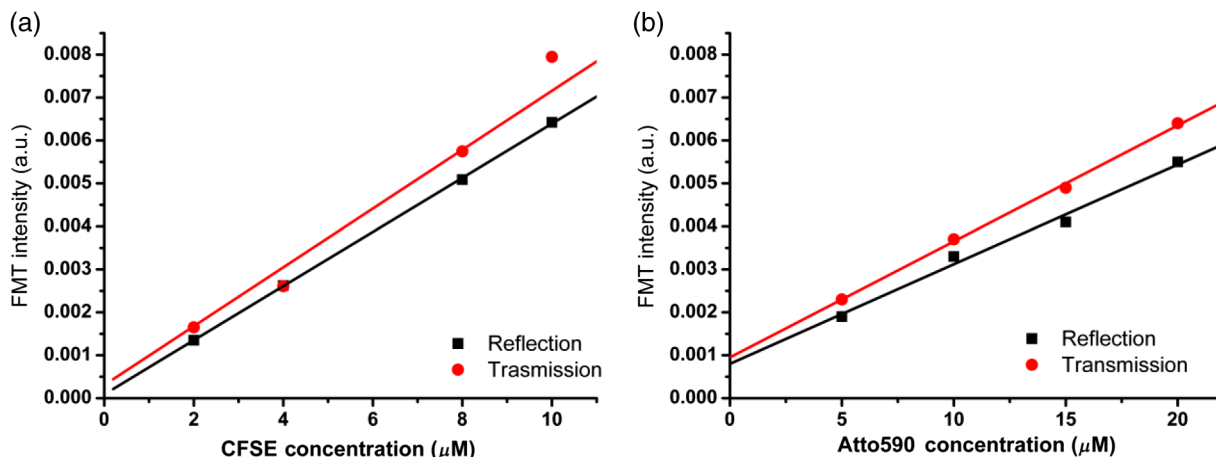


**Fig. 3** Quantification of FMT fluorescent signal in reflection and transmission modalities at different wavelengths. Increasing concentrations of (a) CFSE and (b) Atto590 were measured; fluorescence was detected using the FMT imager in reflection (black) and transmission (red) modalities. The mean intensity values for each experiment were then plotted against the known concentration values and fitted to a linear model.  $R^2 > 0.98$  for all fits (Table 1).

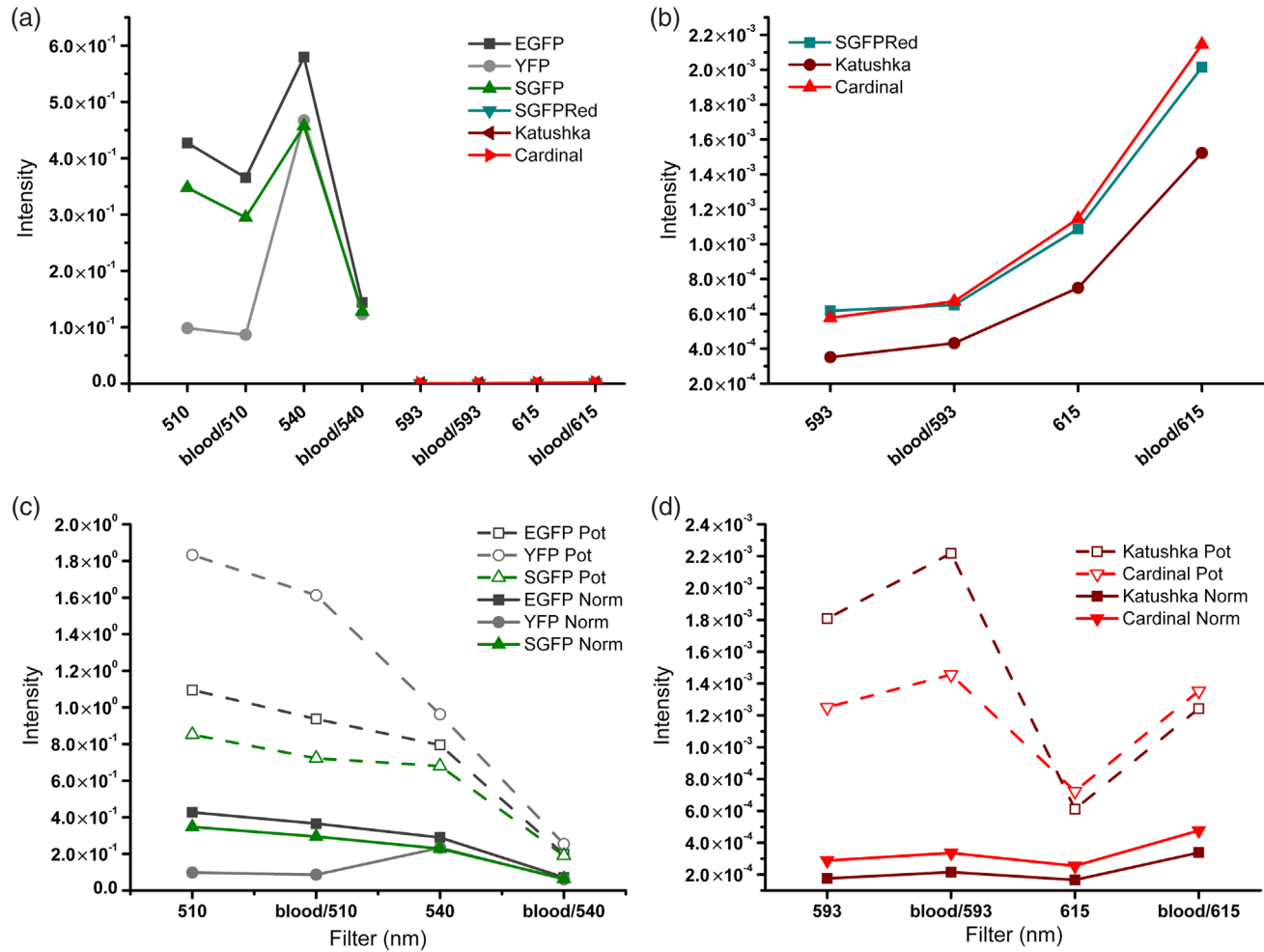


**Fig. 4** Fluorescent protein emission comparison. A 24-well cell culture plate, each containing  $1 \times 10^6$  cells expressing EGFP, SGFP, SYFP, Katushka, and Cardinal, was imaged using the FMT imager with or without addition of 12% heparinated blood. Excitation was performed using 488- and 514-nm laser lines, and fluorescence was recorded with 510/10-, 540/40-, 593/40-, and 615/90-nm filters. (a) Intensity values for each fluorophore were recorded with the optimal filter combination. The intensity values for red emitters are expanded in (b); SGFPRed indicates SGFP-expressing cells detected with the red filter for comparative purposes. The intensity values were normalized to take into account the fluorophore-specific excitation/emission efficiency. The measured normalized values (Norm) and calculated potential values (Pot) are shown for the (c) green and (d) red channels.

For increased spectral resolution, a dedicated spectral imager<sup>2</sup> would be required. Green emitters were approximately 1 order of magnitude brighter than red emitters. The data were further corrected for the “excitation efficiency” term achieved by the available laser lines (488 and 515 nm). To address the nonlinear relationship between excitation wavelength and emission intensity, the values were corrected by an experimentally defined “efficiency factor” as follows:

$$I[\text{Greens}]_{\text{ex } 488} \times (I[\text{ex}_{\text{max}}]/I[\text{ex}_{488}]) \quad (5)$$

and

$$I[\text{Reds}]_{\text{ex } 515} \times (I[\text{ex}_{\text{max}}]/I[\text{ex}_{515}]). \quad (6)$$

$\text{Ex}_{\text{max}}$ ,  $\text{ex}_{488}$ , and  $\text{ex}_{515}$  intensity values were obtained using a fluorimeter, where spectral data were measured using each cell line. Figure 4 shows how, even by exciting at the excitation peak, red emitters still display weak emission and GFP emission is still clearly detectable using a  $>600$ -nm filter. The data were

then corrected for the “emission efficiency” achieved: the emission spectral profiles obtained for the cells were used to calculate the integrals for the whole emission curve and, separately, the integrals for the wavelengths covered by each filter used to image the sample with the FMT as follows:

- 510-nm filter: 505 nm  $\rightarrow$  515 nm;
- 540-nm filter: 520 nm  $\rightarrow$  560 nm;
- 593-nm filter: 573 nm  $\rightarrow$  613 nm; and
- 615-nm filter: 570 nm  $\rightarrow$  660 nm.

The ratio of the “whole emission curve”/“detected emission” represents the portion of fluorescent signal actually detected by the FMT:

$$I[\text{Greens}_{\text{corrected}}] \times \left( \int_{\text{min}}^{\text{max}} \text{emcurve} / \int_{510}^{505} \text{emcurve} \right), \quad (7)$$

or

$$I[\text{Greens}_{\text{corrected}}] \times \left( \int_{\min}^{\max} \text{emicurve} / \int_{520}^{560} \text{emicurve} \right), \quad (8)$$

or

$$I[\text{Reds}_{\text{corrected}}] \times \left( \int_{\min}^{\max} \text{emicurve} / \int_{573}^{613} \text{emicurve} \right), \quad (9)$$

or

$$I[\text{Reds}_{\text{corrected}}] \times \left( \int_{\min}^{\max} \text{emicurve} / \int_{570}^{660} \text{emicurve} \right). \quad (10)$$

The “corrected” values [Figs. 4(c) and 4(d), dashed lines] represent the achievable values by exciting the fluorophores at their excitation maximum and detecting the whole of the emission curve. A final correction that could be made to these values is defined by the QY. This correction should, in theory, equalize the values for the different fluorophores at identical concentrations. Unfortunately, QY information for the specific fluorescent proteins used here was unavailable at the time of writing.

### 3.4 In Vivo Small Animal Imaging

LN represent highly desirable targets for *in vivo* imaging due to their functional importance to the immune system. An immune response is in fact a localized process with LNs acting synergistically while remaining independent from one another. To test whether the FMT could resolve fluorescence from anatomically diverse LNs, the inguinal and mesenteric LNs of a CD2/DsRed mouse were targeted. The inguinal LN is located subcutaneously at the height of the groin, while the MNs are found bunched (usually five to six nodes) deep within the mesentery of the intestine. Figure 5 shows the raw fluorescence data (a) and the 3-D reconstructed image (b) for the right inguinal LN of a CD2/DsRed mouse. The FMT software correctly located the origin of the fluorescent signal, and the reconstructed image matched the dimensions and anatomical conformation of

the inguinal LN. The mesenteric LNs of a CD2/DsRed and a nonfluorescent control mouse were then targeted (Fig. 6). The morphology and location of the MNs make target recognition a difficult task; however, the DsRed-positive reconstructed image displayed three times as much fluorescent signal than the control sample. The bright autofluorescent object visible in both the control and DsRed animals was identified *ex vivo* as the gallbladder. The DsRed signal located at 0.5 to 1 cm below the gallbladder is consistent with the MNs.

## 4 Discussion

The performance of a noncontact FMT system was demonstrated by assessing its quantification accuracy and data reproducibility within 520- to 660-nm windows of the visible spectrum. These data reflect biologically valuable wavelengths, given that most fluorescent proteins and dyes in current use emit light within that range. These wavelengths are particularly challenging for quantitative optical imaging setups, given that the contribution of autofluorescence, scattering, and absorption by biological tissues is nonlinear. It is useful to note that although NIR fluorescent proteins and probes have been developed over the past decade, their use in biological applications is still lagging compared with well-established green fluorescent proteins such as GFP, and the use of many markers, including fluorescently labeled antibodies, used in fluorescence microscopy has not been widely translated to an *in vivo* setting. The nonlinear attenuation of light transmission in turn affects the ability to compare fluorescence emissions from different anatomical regions. In practice, this means that, in a typical experimental design, fluorophores are compared with a control sample group (e.g., before and after a treatment) and only rarely to a spectrally distinct fluorophore. It is therefore important to establish a method that enables the quantitative detection of fluorescence, regardless of anatomical location and wavelength. Reconstructed FMT intensities were here found to be linearly dependent on fluorophore concentration, and this result was reproduced irrespective of wavelength and acquisition geometry, strengthening the notion that FMT can accurately retrieve

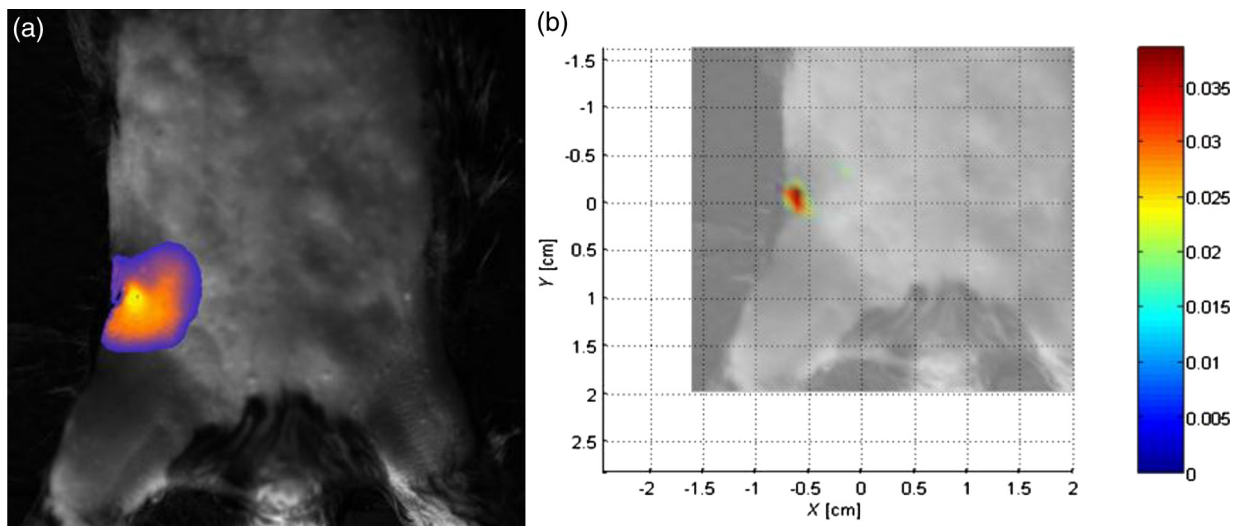


**Fig. 5** Subcutaneous localization and FMT rendering of the inguinal LN of a CD2/DsRed mouse. (a) Fluorescence tomography raw data (514 nm excitation; 615/90 nm emission), and (b) FMT 3-D reconstruction shows how the rendering process correctly localizes the shape and location of the LN.

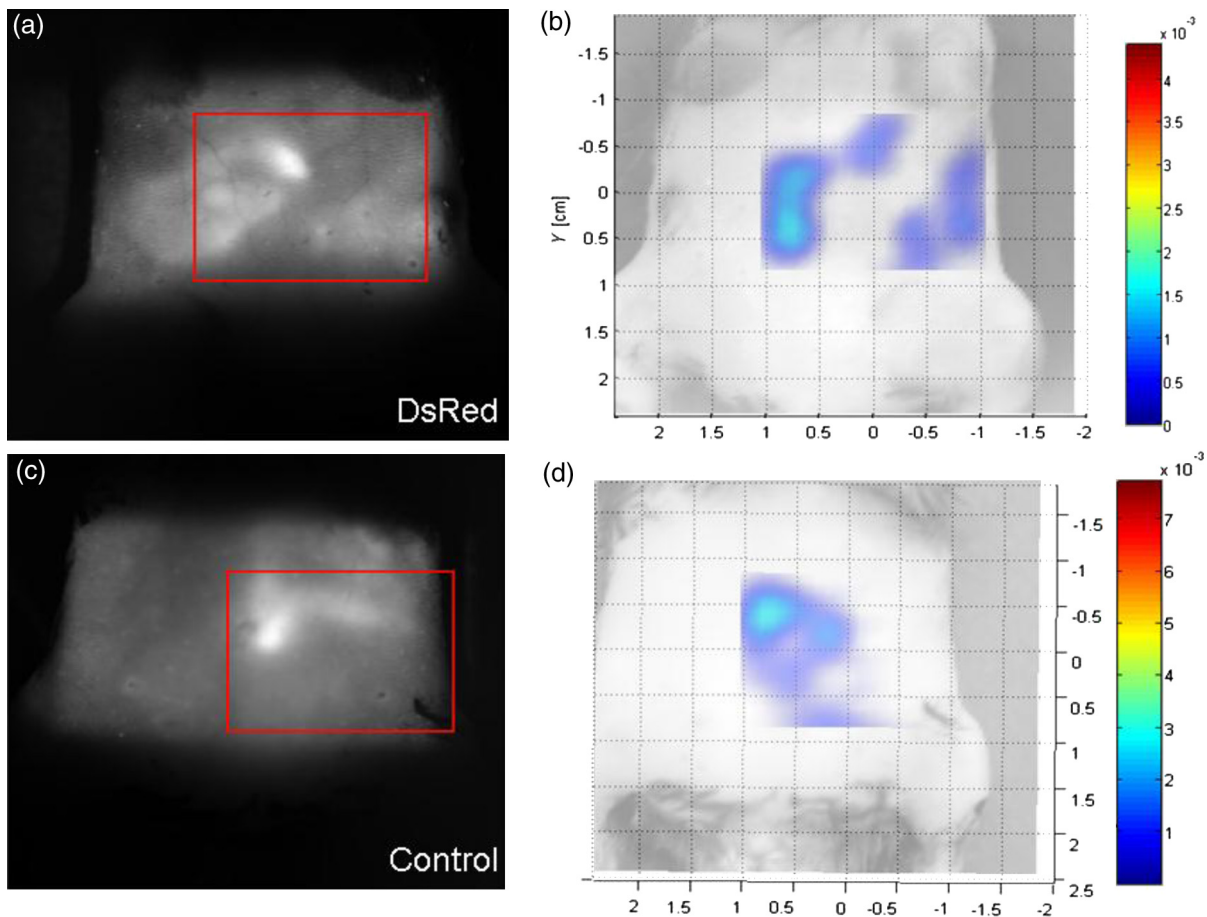


**Fig. 6** FMT localization and rendering of the mesenteric LNs of a CD2/DsRed mouse. 2-D homogeneous illumination images of the ventral area of (a) a CD2/DsRed and (c) a control mouse show the spatial spread of fluorescent and autofluorescent objects. The area delimited by the red boxes represents the area selected for the 3-D FMT rendering (b and d) for each mouse. The difference in anatomical location of nontarget autofluorescent objects illustrates the challenges faced in the FMT reconstructions.

concentration values for subsurface and deeper-seated ROIs. The reproducibility of the FMT data was evaluated by three parameters: (1) the SNR was optimized experimentally to reduce variance between background and target-specific emissions; (2) SDM between FMT intensity and fluorophore concentration was used as an indicator of dynamic range; and (3) SDM of repeated measurements was used as an indicator of technical accuracy. Standard deviation and standard error values throughout this study were consistently found to be at least 1 to 2 orders of magnitude smaller than the mean intensity value across intensities. A protocol for the calibration of the FMT system was established that allowed converting FMT intensity values to fluorophore concentrations, with accuracy values that reflected experimental variability. Repeated measurements were performed, and the variance between measurements was found to be  $10^{-2}$  to  $10^{-3} < \text{mean}$ . FMT quantification accuracy within the visible spectrum was therefore in the nanomolar range and formalized by the variance coefficient at  $<1\%$ . The relative strength of five fluorophores was evaluated in the presence of blood in order to mimic the most challenging *in vivo* settings. The absorption properties of the heme group around 500 nm significantly affected the excitation light penetration. During data processing, the normalization of excitation and emission light resulted in an apparent increase of fluorescence in the presence of blood, dictated by a difference in absorbed excitation

light. It is clear from these data that FP performance should be experimentally validated for each application and imaging setup characteristic. Most red emitters were found to be approximately 1 order of magnitude less bright than EGFP and EYFP; therefore, in cases where excitation/emission excitation was suboptimal, red FPs could be outperformed by green FPs. The translational potential of these results to an *in vivo* setting was demonstrated here by the detection and reconstruction of fluorescently labeled T-cells *in vivo*. The FMT imager correctly located two spectrally and anatomically distinct regions: the inguinal LNs and the MNs of a transgenic CD2/DsRed mouse. The quantification accuracy of the fluorescent reconstructions *in vivo* was assessed separately using flow cytometry data.<sup>27</sup> Cumulatively, the data demonstrate that noncontact FMT can perform quantitative fluorescence imaging *in vitro* and *in vivo* in a window of the visible spectrum with high precision and provide the advantage of quantitatively comparing fluorescent emissions across a wide spectral window, regardless of anatomical location.

#### Acknowledgments

This work was supported by the FP7 EU Grant “FMT-XCT.” RF acknowledges support from the Marie Curie Early Stage Training Grant “EST-MolecImag.”

## References

1. A. Garofalakis et al., "In vivo validation of free-space fluorescence tomography using nuclear imaging," *Opt. Lett.* **35**(18), 3024–3026 (2010).
2. G. Zacharakis et al., "Spectroscopic detection improves multi-color quantification in fluorescence tomography," *Biomed. Opt. Express* **2**(3), 431–439 (2011).
3. D. Vonwil et al., "Validation of fluorescence molecular tomography/micro-CT multimodal imaging in vivo in rats," *Mol. Imaging Biol.* **16**(3), 350–361 (2014).
4. V. Ntziachristos et al., "Concurrent MRI and diffuse optical tomography of breast after indocyanine green enhancement," *Proc. Natl. Acad. Sci. U. S. A.* **97**(6), 2767–2772 (2000).
5. J. Ripoll and V. Ntziachristos, "From finite to infinite volumes: removal of boundaries in diffuse wave imaging," *Phys. Rev. Lett.* **96**(17), 173903 (2006).
6. J. Ripoll, R. B. Schulz, and V. Ntziachristos, "Free-space propagation of diffuse light: theory and experiments," *Phys. Rev. Lett.* **91**(10), 103901 (2003).
7. H. Meyer et al., "Noncontact optical imaging in mice with full angular coverage and automatic surface extraction," *Appl. Opt.* **46**(17), 3617–3627 (2007).
8. A. Soubret, J. Ripoll, and V. Ntziachristos, "Accuracy of fluorescent tomography in the presence of heterogeneities: study of the normalized Born ratio," *IEEE Trans. Med. Imaging* **24**(10), 1377–1386 (2005).
9. R. B. Schulz, J. Ripoll, and V. Ntziachristos, "Noncontact optical tomography of turbid media," *Opt. Lett.* **28**(18), 1701–1703 (2003).
10. V. Ntziachristos et al., "Visualization of antitumor treatment by means of fluorescence molecular tomography with an annexin V-Cy5.5 conjugate," *Proc. Natl. Acad. Sci. U. S. A.* **101**(33), 12294–12299 (2004).
11. J. Ripoll et al., "Experimental determination of photon propagation in highly absorbing and scattering media," *J. Opt. Soc. Am. A* **22**(3), 546–551 (2005).
12. G. Zacharakis et al., "Volumetric tomography of fluorescent proteins through small animals in vivo," *Proc. Natl. Acad. Sci. U. S. A.* **102**(51), 18252–18257 (2005).
13. G. Zacharakis et al., "Fluorescent protein tomography scanner for small animal imaging," *IEEE Trans. Med. Imaging* **24**(7), 878–885 (2005).
14. A. Garofalakis et al., "Three-dimensional in vivo imaging of green fluorescent protein-expressing T cells in mice with noncontact fluorescence molecular tomography," *Mol. Imaging* **6**(2), 96–107 (2007).
15. S. R. Arridge, "Optical tomography in medical imaging," *Inverse Probl.* **15**, R41–R93 (1999).
16. J. Ripoll and V. Ntziachristos, "Imaging scattering media from a distance: theory and applications of non-contact optical tomography," *Mod. Phys. Lett. B* **18**, 1403–1431 (2004).
17. V. Ntziachristos et al., "In vivo tomographic imaging of near-infrared fluorescent probes," *Mol. Imaging* **1**, 82–88 (2002).
18. V. Ntziachristos and R. Weissleder, "Experimental three-dimensional fluorescence reconstruction of diffuse media using a normalized Born approximation," *Opt. Lett.* **26**, 893–895 (2001).
19. E. E. Graves et al., "Validation of in vivo fluorochrome concentrations measured using fluorescence molecular tomography," *J. Biomed. Opt.* **10**(4), 044019 (2005).
20. C. Kak and M. Slaney, *Principles of Computerized Tomographic Imaging*, IEEE, New York (1988).
21. S. R. Arridge and M. Schweiger, "Image reconstruction in optical tomography," *Philos. Trans. R. Soc. Lond. B* **352**(1354), 717–726 (1997).
22. J. Ripoll et al., "Fast analytical approximation for arbitrary geometries in diffuse optical tomography," *Opt. Lett.* **27**(7), 527–529 (2002).
23. A. Sarasa-Renedo et al., "Source intensity profile in noncontact optical tomography," *Opt. Lett.* **35**(1), 34–36 (2010).
24. M. Simantiraki et al., "Multispectral unmixing of fluorescence molecular tomography data," *J. Innovative Opt. Health Sci.* **2**(4), 353–364 (2009).
25. S. Psycharakis et al., "Autofluorescence removal from fluorescence tomography data using multispectral imaging," *Proc. SPIE* **6626**, 66260I (2007).
26. I. Weidenfeld et al., "Inducible expression of coding and inhibitory RNAs from retargetable genomic loci," *Nucleic Acids Res.* **37**(7), e50 (2009).
27. R. Favicchio et al., "Kinetics of T-cell receptor-dependent antigen recognition determined in vivo by multi-spectral normalized epifluorescence laser scanning," *J. Biomed. Opt.* **17**(7), 076013 (2012).
28. S. R. Arridge, M. Schweiger, and D. T. Delpy, "Iterative reconstruction of near-infrared absorption images," *Proc. SPIE* **1767**, 372–383 (1992).
29. D. Shcherbo et al., "Bright far-red fluorescent protein for whole-body imaging," *Nat. Methods* **4**(9), 741–746 (2007).
30. J. Chu et al., "Non-invasive intravital imaging of cellular differentiation with a bright red-excitable fluorescent protein," *Nat. Methods* **11**(5), 572–578 (2014).
31. E. Spanopoulou et al., "The homeodomain region of Rag-1 reveals the parallel mechanisms of bacterial and V(D)J recombination," *Cell* **87**(2), 263–276 (1996).
32. E. Spanopoulou et al., "Functional immunoglobulin transgenes guide ordered B-cell differentiation in Rag-1-deficient mice," *Genes Dev.* **8**(9), 1030–1042 (1994).
33. J. de Boer et al., "Transgenic mice with hematopoietic and lymphoid specific expression of Cre," *Eur. J. Immunol.* **33**(2), 314–325 (2003).
34. H. Veiga-Fernandes et al., "Tyrosine kinase receptor RET is a key regulator of Peyer's patch organogenesis," *Nature* **446**(7135), 547–551 (2007).

**Rosy Favicchio**, PhD, is a molecular biologist who specializes in the development of *in vivo* imaging technologies for the study of biological dynamics with a keen interest in metabolism. She is currently a research fellow at Imperial College London where she is developing theranostic tools applied to cancer research.

**Stylianos Psycharakis** is currently a PhD student at the University of Crete and a member of the *In vivo* Imaging Lab, Institute of Electronic Structure & Laser, Foundation for Research and Technology—Hellas, Heraklion Crete, Greece. His research interests include the design and realization of novel 3-D Microscopic imaging techniques such as Selective Plane Illumination Microscopy and Optical Projection Tomography and their application in studying dynamic biological processes.

Biographies for the other authors are not available.